Effect of Pressure on the Complete Phase Behavior of Binary Mixtures

Monica H. Lamm and Carol K. Hall
Dept. of Chemical Engineering, North Carolina State University, Raleigh, NC 27695

Using Gibbs-Duhem integration and semigrand canonical Monte Carlo simulations, temperature vs. composition phase diagrams for a binary Lennard-Jones mixture, $\sigma_{11}/\sigma_{22} = 0.85$ and $\epsilon_{11}/\epsilon_{22} = 1.6$, are calculated at several reduced pressures in order to examine the effects of pressure on complete phase behavior (that is, equilibrium between vapor, liquid, and solid phases). Interference is observed between the vapor–liquid and solid–liquid coexistence regions at the lowest pressure. As the pressure increases, the vapor–liquid coexistence region shifts to higher temperatures, while the solid–liquid coexistence region remains essentially unaffected. Eventually, the vapor–liquid coexistence region lifts off the solid–liquid coexistence region, ending the interference. Pressure vs. temperature projections for binary Lennard-Jones mixtures at $\sigma_{11}/\sigma_{22} = 0.85$, 0.9, and 0.95, and $\epsilon_{11}/\epsilon_{22} = 0.45$ and 1.6 are also presented to explore how the three-phase loci (solid–liquid–vapor and solid–solid–liquid) change with variations in diameter ratio and well-depth ratio. It is found that as the diameter ratio decreases, the maximum pressure in the solid–liquid–vapor locus decreases and the characteristic shape of the solid–liquid coexistence region changes from peritectic to eutectic. As the well-depth ratio decreases, the maximum pressure in the solid–liquid–vapor locus increases. For one mixture, $\sigma_{11}/\sigma_{22} = 0.9$ and $\epsilon_{11}/\epsilon_{22} = 1.6$, a quadruple point of solid–solid–liquid–vapor coexistence is located. © 2004 American Institute of Chemical Engineers *AIChE J,* 50: 215–225, 2004
Keywords: simulation, molecular, phase equilibrium, computer simulations (MC and MD)

Introduction

Understanding the vapor-, liquid-, and solid-phase behavior of mixtures is a prerequisite for designing extraction and crystallization processes. Most of the research aimed at understanding how intermolecular interactions affect phase behavior has focused on fluid-phase equilibria, although in real systems solid phases form and often interrupt the complex phase behavior exhibited by fluids (Schneider, 1978; Scott, 1987). Phenomenological descriptions of complete phase behavior (that is, showing equilibrium between vapor, liquid, and solid phases) were given by Luks (1980), Peters et al. (1986), and Valyashko (1986, 1990). Luks and Peters et al. described four types of complete phase diagrams observed for binary mixtures of solvent (methane, ethane, carbon dioxide) and a homologous series of solutes (*n*-alkanes). Valyashko proposed a classification scheme for 12 types of complete diagrams. Eight of these types result from the analysis of experimental data for water–inorganic salt mixtures. The remaining four types were deduced by the method of continuous topological transformation, which involves making educated guesses about the transitions in topography between the eight known types. This is based on the likely-correct assumption that there are continuous transitions between all types of phase behavior (Schneider, 1970).

A quantitative description of complete phase behavior was given by Luks and coworkers (Garcia and Luks, 1999; Labadie et al., 2000). Garcia and Luks (1999) calculated the solid–liquid–vapor locus for binary mixtures of solvent and a homologous series of solutes using the van der Waals equation of state for the fluid phase and a simple fugacity model for the

Correspondence concerning this article should be addressed to C. K. Hall at hall@turbo.che.wcsu.edu.
Current address of M. H. Lamm: Dept. of Chemical Engineering, Iowa State University, Ames, IA 50011; e-mail: mhlamm@iastate.edu.

solid phase. This work was extended by Labadie et al. (2000) who calculated the fluid-phase critical loci for these mixtures, offering a picture of how the multiphase topography progresses with changes in the solute properties. They found examples of solid–fluid-phase behavior in keeping with what has been observed in real systems, as well as solid–fluid-phase behavior that has yet to be verified by experiment. As with any analytical equation of state, there exists the possibility that the new topographies are mathematical artifacts stemming from the approximations made in the development of the equation of state. Nonetheless, the new possibilities for complete phase behavior calculated by Luks and coworkers are intriguing and invite further investigation.

In a previous article (Lamm and Hall, 2001) we used the Gibbs-Duhem integration method combined with semigrand canonical Monte Carlo simulations to calculate complete phase diagrams for binary Lennard-Jones mixtures over a range of diameter ratios $\sigma_{11}/\sigma_{22} = 0.85 - 1.0$ and well-depth ratios $\epsilon_{11}/\epsilon_{22} = 0.625 - 1.6$ at a single reduced pressure. The cross-species interaction parameters were calculated using the Lorentz-Berthelot (Rowlinson and Swinton, 1982) combining rules. We restricted our study to diameter ratios ranging from 0.85 to 1.0, because calculations on binary hard-sphere mixtures have shown that the stable solid phase in this region is a substitutionally disordered fcc crystal (Barrat et al., 1986, 1987; Kranendonk and Frenkel, 1991; Cottin and Monson, 1995). At diameter ratios of less than 0.85, the phase-equilibrium calculation becomes more complex, because several ordered crystalline phases are possible, necessitating the calculation of each phase's free energy to determine the most stable crystalline structure. We found that for well-depth ratios of unity (equal attractions among species) there is no interference between the vapor–liquid and solid–liquid coexistence regions. As the well-depth ratio increases or decreases from unity, the vapor–liquid and solid–liquid phase envelopes become wider and interfere with each other, leading to a solid–vapor coexistence region. For all well-depth ratios and a diameter ratio of 0.95, the solid–liquid lines have a shape characteristic of a solid solution (with or without a minimum melting temperature); as the diameter ratio decreases, the solid–liquid lines fall to lower temperatures until they eventually drop below the solid–solid coexistence region, resulting in either a eutectic or peritectic three-phase (solid–solid–liquid) line.

In this article we explore the effect of pressure on the complete phase behavior of a mixture. The complete phase diagrams are calculated using Gibbs-Duhem integration combined with semigrand canonical Monte Carlo simulation; this procedure has been described in detail elsewhere (Lamm and Hall, 2001). We present phase diagrams for six binary Lennard-Jones mixtures with $\sigma_{11}/\sigma_{22} = 0.85$, 0.9, and 0.95, and $\epsilon_{11}/\epsilon_{22} = 0.45$ and 1.6. We begin with a detailed description of the $T - x$ phase diagrams for the binary Lennard-Jones mixture with diameter ratio $\sigma_{11}/\sigma_{22} = 0.85$ and well-depth ratio $\epsilon_{11}/\epsilon_{22} = 1.6$ at reduced pressures $P^* = 0.002$, 0.01, 0.025, 0.05, and 0.1. These results are then summarized on a P–T projection that identifies the three-phase coexistence features of the mixture (solid–liquid–vapor and solid–solid–liquid) in addition to the pure component vapor–liquid, solid–liquid, and vapor–solid coexistence curves. We then present similar P–T projections for the remaining mixtures and discuss how the three-phase lines (solid–liquid–vapor and solid–solid–liquid) change with variations in diameter ratio σ_{11}/σ_{22} and well-depth ratio $\epsilon_{11}/\epsilon_{22}$.

Highlights of our simulation results are the following. For the mixture with $\sigma_{11}/\sigma_{22} = 0.85$ and $\epsilon_{11}/\epsilon_{22} = 1.6$, the vapor–liquid and solid–liquid coexistence regions interfere on the T–x diagram at low pressure ($P^* = 0.002$). As pressure increases, the vapor–liquid coexistence region first shifts to higher temperatures and then begins to disappear as the pressure approaches critical conditions. These results are summarized on a pressure–temperature phase diagram that identifies the three-phase coexistence features of the mixture (solid–liquid–vapor, solid–solid–liquid) in addition to the pure-component vapor–liquid, solid–liquid, and vapor–solid coexistence curves. Pressure–temperature diagrams are presented for five additional mixtures. For one mixture, $\sigma_{11}/\sigma_{22} = 0.9$ and $\epsilon_{11}/\epsilon_{22} = 1.6$, we locate a quadruple (solid(1)–solid(2)–liquid–gas) coexistence point. Upon comparing the P–T projections for each mixture, we find that as the diameter ratio decreases, the maximum in the locus of solid–liquid–vapor coexistence pressures decreases and the locus of solid(1)–solid(2)–liquid temperatures shifts from temperatures above the solid–liquid temperature of pure component 1 to temperatures below the solid–liquid coexistence temperature of pure component 1. We find that as well-depth ratio decreases, the coexistence curves for pure component 2 shift from temperatures and pressures below those of pure component 1 to temperatures and pressures above those of pure component 1 and that the maximum in the locus of solid–liquid–vapor coexistence pressures increases.

This article is organized as follows. The Gibbs-Duhem integration method is outlined for two- and three-phase coexistence lines. The results of our calculations of complete T-X phase diagrams are presented for the binary mixture, $\sigma_{11}/\sigma_{22} = 0.85$, $\epsilon_{11}/\epsilon_{22} = 1.6$, at five reduced pressures, $P^* = 0.002$, 0.01, 0.025, 0.05, and 0.1, in order to observe how the shape of the curves on the T–x diagram change with variation in pressure. P–T projections are also presented for binary mixtures with $\sigma_{11}/\sigma_{22} = 0.85$, 0.9, and 0.95, and $\epsilon_{11}/\epsilon_{22} = 0.45$ and 1.6 to examine how these diagrams change with variations in Lennard-Jones diameter ratio and well-depth ratio. We conclude with a brief summary and further discussion.

Method

In this section we describe how we calculated phase equilibria for binary Lennard-Jones mixtures using the Gibbs-Duhem integration method. We begin by presenting a brief review of the Gibbs-Duhem integration method. We then discuss our procedures for determining an initial coexistence condition and integrating the Clapeyron equation. Finally, we describe the details of the semigrand ensemble simulations used throughout the integration procedure to determine the properties of each of the coexisting phases.

The coexistence lines were calculated using Gibbs-Duhem integration (Kofke, 1993, 1998). In this method, phase coexistence is determined by numerically integrating the Clapeyron differential equation appropriate to the system of interest. Clapeyron equations describe how field variables (variables that must be equal among coexisting phases) change along the phase-equilibrium line. The Clapeyron equation for equilibrium between two phases (α and γ) of a binary mixture con-

taining components 1 and 2 at constant pressure is (see Appendix)

$$\frac{d\beta}{d\xi_2} = \frac{(x_2^\alpha - x_2^\gamma)}{\xi_2(1-\xi_2)(h^\alpha - h^\gamma)}, \tag{1}$$

where β is the reciprocal temperature, $1/kT$, with k the Boltzmann constant and T the absolute temperature; ξ_2 is the fugacity fraction of species 2; $\xi_2 \equiv \hat{f}_2/\Sigma\hat{f}_i$, with $\hat{f}_i$, the fugacity of species i in solution; x_2 is the mole fraction of species 2; and h is the molar enthalpy. The righthand side of Eq. 1 can be integrated numerically to find an equation for β as a function of ξ_2 if we have an initial condition describing the temperature, fugacity fraction, enthalpies, and compositions at one coexistence point.

Initial condition

An initial coexistence condition is necessary to begin a Gibbs-Duhem integration calculation for phase equilibrium in a binary mixture. A convenient choice for the initial coexistence condition is the vapor–liquid or solid–liquid equilibrium condition for either of the pure Lennard-Jones components. Here, we used data from the literature obtained via Gibbs-Duhem integration for the vapor–liquid (Kofke, 1993) and solid–liquid (Agrawal and Kofke, 1995) coexistence conditions. The integrand in Eq. 11 is undefined for pure components ($\xi_2 = 0$, $x_2 = 0$ and $\xi_2 = 1$, $x_2 = 1$), but it can be estimated using the limiting case of infinite dilution. We follow the procedure of Mehta and Kofke (1994), who used the infinite-dilution case to start their Gibbs-Duhem integration calculations of vapor–liquid equilibria in binary mixtures.

The limiting value of the integrand when x_2 approaches zero, $(d\beta/d\xi_2)_{x_2=0}$, can be estimated by supposing that the real mixture displays ideal solution behavior at the limit of infinite dilution of species 2. With this assumption, the abundant component (species 1) in the ideal solution follows the Lewis Randall rule

$$\hat{f}_1 = x_1 f_1, \tag{2}$$

while the dilute component (species 2) obeys Henry's law

$$\hat{f}_2 = x_2 H_2, \tag{3}$$

where f_1 is the fugacity of pure component 1 at the temperature and pressure of the mixture, and H_2 is the Henry's law constant for species 2. Letting $x_1 \to 1$ and $x_2 \to 0$, the fugacity fraction of species 2 becomes, $\xi_2 = x_2 H_2/f_1$. After making these substitutions into Eq. 1 and rearranging terms (Hitchcock and Hall, 1999), we get

$$\left.\frac{d\beta}{d\xi_2}\right|_{x_2=0} = \frac{f_1(1/H_2^\alpha - 1/H_2^\gamma)}{(h^\alpha - h^\gamma)}. \tag{4}$$

This gives us an estimate for the integrand at the initial condition of $\xi_2 = 0$ and coexistence (e.g., solid–liquid, vapor–liquid) temperature of pure species 1. A similar formula can be derived in the limit of infinite dilution of species 1.

We can calculate all of the quantities on the righthand side of Eq. 4 with an NPT simulation of pure species 1. The molar enthalpy of each phase is $h = \langle u + Pv\rangle_{NPT}$, where u is the configurational energy of the system and the brackets, $\langle\ \ \rangle_{NPT}$, denote an NPT ensemble average. The quantity f_1/H_2 can be calculated from (Mehta and Kofke, 1994)

$$\frac{f_1}{H_2} = \langle \exp(-\beta \Delta u_{1\to 2})\rangle_{NPT} \tag{5}$$

where $\Delta u_{1\to 2}$ is the exchange energy associated with switching a particle from species 1 to species 2. The exchange energy, $\Delta u_{1\to 2}$, can be obtained by conducting trial identity switches during a simulation at infinite dilution of species 2; these involve randomly selecting a particle and calculating the energy that would result if we were to switch the particle from species 1 to species 2. This is done without actually changing the particle's identity.

Integration along coexistence lines

Once we have an initial coexistence condition, the Gibbs-Duhem integration procedure can be performed over the entire range of fugacity fractions, $\xi_2 = 0$ to $\xi_2 = 1$, using a predictor–corrector algorithm to integrate Eq. 1. Starting at the initial condition, β_0, $(\xi_2)_0$, we step to the next fugacity fraction, $(\xi_2)_1$, and estimate the associated reciprocal temperature, β_1, using the trapezoid-rule predictor formula

$$\beta_1^{(0)} = \beta_0 + [(\xi_2)_1 - (\xi_2)_0]F(\beta_0, (\xi_2)_0) \tag{6}$$

where the superscript "0" indicates that $\beta_1^{(0)}$ (a predicted value) is our zeroth iteration attempt at finding the reciprocal temperature β_1 and F is the righthand side of Eq. 1 evaluated at the initial condition. Once $\beta_1^{(0)}$ is estimated at the given fugacity fraction $(\xi_2)_1$, two semigrand canonical (NPTξ_2) Monte Carlo simulations (one for the α phase and one for the γ phase) are conducted in order to calculate the enthalpies and mole fractions of each phase at the new state point. (Details of the NPTξ_2 simulations will be given in the following section.)

After the enthalpies and mole fractions at the new state point are calculated, we refine the estimate for β_1 at $(\xi_2)_1$ by performing a loop of corrector iterations until β_1 converges within an acceptable tolerance. The general form of the trapezoid-rule corrector for this loop is given by

$$\beta_1^{(i+1)} = \beta_0 + \frac{[(\xi_2)_1 - (\xi_2)_0]}{2}[F_1^{(i)}(\beta_1^{(i)}, (\xi_2)_1) + F_0(\beta_0, (\xi_2)_0)] \tag{7}$$

where the superscripts (i) and $(i+1)$ denote the iterations of the corrector, the subscripts "0" and "1" denote the initial and current state point, respectively, and $F_1^{(i)}$ is calculated from simulation averages of the enthalpies and mole fractions during the ith iteration of the corrector at $\beta_1^{(i)}$ and $(\xi_2)_1$. After β_1 converges, a production segment of simulations is run to obtain the final average enthalpies and mole fractions for the coexistence point. Once the production runs are completed, the fugacity fraction is incremented and the predictor–corrector algo-

rithm just described is repeated to obtain the next state point, β_2, $(\xi_2)_2$.

Higher-order predictor–corrector equations are used as we obtain more state points. The midpoint predictor–corrector is used once two state points are known

$$\beta_{n+1}^{(0)} = \beta_{n-1} + 2[(\xi_2)_{n+1} - (\xi_2)_n]F_n(\beta_n, (\xi_2)_n), \quad (8)$$

$$\beta_{n+1}^{(i+1)} = \beta_{n-1} + \frac{[(\xi_2)_{n+1} - (\xi_2)_n]}{3}[F_{n+1}^{(i)} + 4F_n + F_{n-1}] \quad (9)$$

and the modified Adams predictor–corrector (Carnahan et al., 1969) is used once three or more state points are known

$$\beta_{n+1}^{(0)} = \beta_n + \frac{[(\xi_2)_{n+1} - (\xi_2)_n]}{24} \times [55F_n - 59F_{n-1} + 37F_{n-2} - 9F_{n-3}] \quad (10)$$

$$\beta_{n+1}^{(i+1)} = \beta_n + \frac{[(\xi_2)_{n+1} - (\xi_2)_n]}{24} \times [9F_{n+1}^{(i)} + 19F_n - 5F_{n-1} + F_{n-2}] \quad (11)$$

In these sets of equations the predictor is listed first and the corrector second. The subscripts denote the coexistence state points, with $(n + 1)$ being the current state point and the superscripts denote the iterations of the corrector with $(i + 1)$ being the current iteration of β for the coexistence state point. By repeating the predictor–corrector algorithm from $\xi_2 = 0$ to $\xi_2 = 1$, we can map out the entire temperature vs. composition phase diagram.

Simulation in the semigrand canonical ensemble

The enthalpies and mole fractions needed as input to the integration of Eq. 1 are obtained from semigrand canonical (constant NPTξ_2) Monte Carlo computer simulations (Kofke and Glandt, 1988). In this work, all simulations were run with a system size of 500 particles. The temperature, pressure, and fugacity fraction were fixed at the values specified by the Gibbs-Duhem integration predictor–corrector algorithm. There are three types of Monte Carlo trial moves in semigrand canonical simulations: particle displacements, volume-change moves, and particle-identity exchanges. The particle displacements and volume-change moves are conducted just as they are in a standard NPT simulation (Allen and Tildesley, 1987). In the particle identity exchange moves, a particle is selected at random and given a trial species identity switch, which is accepted according to the ratio of the species fugacity fractions, ξ_1 and ξ_2. The overall acceptance probability (Mehta and Kofke, 1994) for the moves in the NPTξ_2 ensemble is min[1, exp(Λ)], where

$$\Lambda = -\beta(U^{\text{trial}} - U^{\text{old}}) - \beta P(V^{\text{trial}} - V^{\text{old}}) + N \ln \frac{V^{\text{trial}}}{V^{\text{old}}} + m \ln \frac{\xi_2}{1 - \xi_2} \quad (12)$$

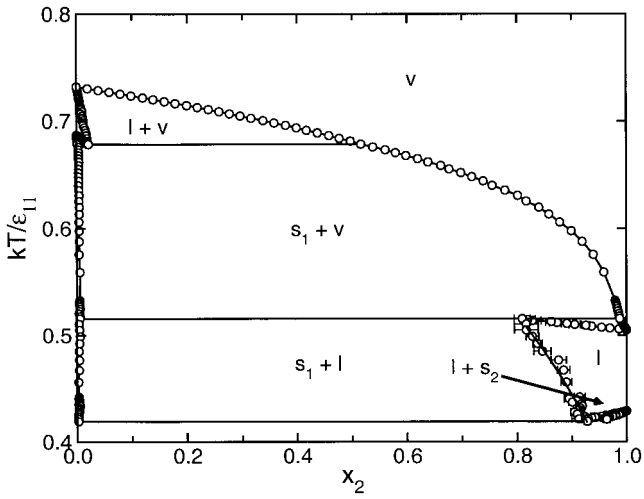

Figure 1. Temperature vs. composition-phase diagram for a binary Lennard-Jones mixture with diameter ratio $\sigma_{11}/\sigma_{22} = 0.85$ and $\epsilon_{11}/\epsilon_{22} = 1.6$ at $P^* = 0.002$.

The circles represent data from Gibbs-Duhem integration simulations. Error bars are shown when they are larger than the width of the symbol. Lines are drawn through the points for clarity. The labels identifying the phases present in each region are as follows: v (vapor), l (liquid), and s_i (fcc solid solution rich in component i).

In Eq. 12, U^{trial} and U^{old}, and V^{trial} and V^{old}, are the configurational energies and volumes of the trial and existing states, respectively, $m = +1$ if the trial identity switch is from species 1 to 2, and $m = -1$ if the trial identity switch is from species 2 to 1. In NPTξ_2 simulations the choice of the type of Monte Carlo move is made randomly, but weighted such that the ratio of attempted moves is one volume change to N particle displacements to N identity switches. The length of the simulation is given in cycles, where one cycle represents 1 volume change attempt, N displacement attempts, and N identity switch attempts. In our work, a typical NPTξ_2 simulation is equilibrated for 3000 cycles and then followed by a production run of 5000 cycles to compute the average enthalpy and mole fraction. The only difference between fluid- and solid-phase simulations is that to maintain an fcc crystalline structure in the solid phase simulations we impose a single occupancy constraint (Hansen and McDonald, 1969; Kofke, 1991) on the trial displacements of particles in the solid, that is, any displacements that put the particle outside its lattice cell are rejected.

Other details of the NPTξ_2 simulations are as follows. The simulation volume is a cubic box with periodic boundary conditions. The particles interact via the Lennard-Jones potential model. We determine the cross-species interaction parameters (σ_{12}, ϵ_{12}) by using the Lorentz-Berthelot (Rowlinson and Swinton, 1982) combining rules $\sigma_{12} = (\sigma_{11} + \sigma_{22})/2$ and $\epsilon_{12} = \sqrt{\epsilon_{11}\epsilon_{22}}$. The potential interactions are truncated at a cutoff radius of half the box length. To compensate for this truncation, a long range correction is applied to the energy calculations during the simulation by assuming a uniform density distribution beyond the cutoff radius (Allen and Tildesley, 1987).

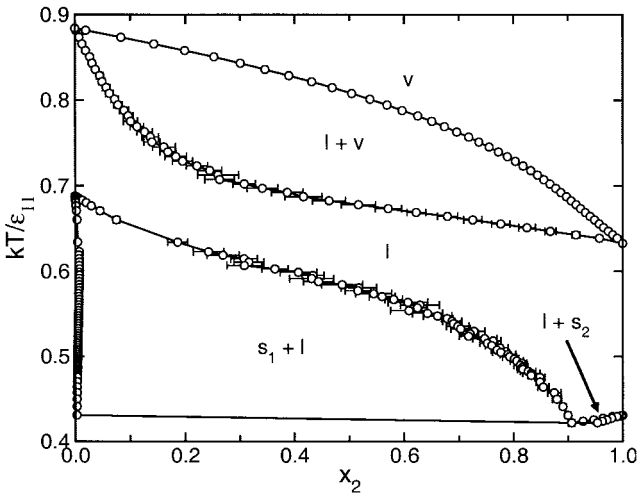

Figure 2. Temperature vs. composition-phase diagram for a binary Lennard-Jones mixture with diameter ratio σ_{11}/σ_{22} = 0.85 and $\epsilon_{11}/\epsilon_{22}$ = 1.6 at P^* = 0.01: symbols as in Figure 1.

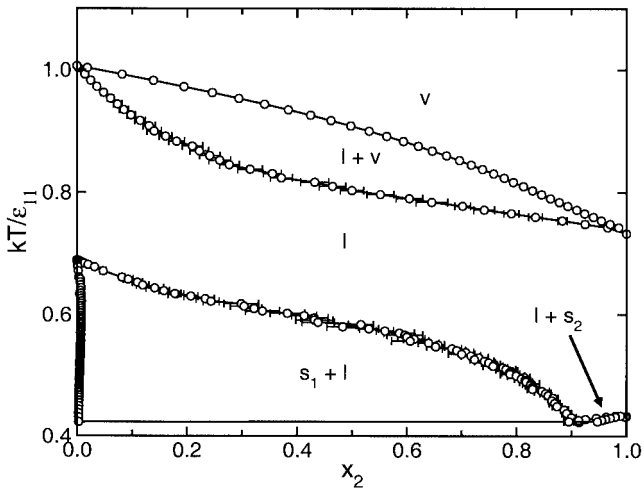

Figure 3. Temperature vs. composition-phase diagram for a Lennard-Jones binary mixture with diameter ratio σ_{11}/σ_{22} = 0.85 and $\epsilon_{11}/\epsilon_{22}$ = 1.6 at P^* = 0.025: symbols as in Figure 1.

T–x Phase Diagrams for Binary Mixtures

A phase diagram in the T–x plane is shown in Figure 1 for the binary Lennard-Jones mixture with $\sigma_{11}/\sigma_{22} = 0.85$ and $\epsilon_{11}/\epsilon_{22} = 1.6$ at $P^* \equiv P\sigma_{11}^3/\epsilon_{11} = 0.002$, which is equivalent to atmospheric pressure if the Lennard-Jones model parameters for argon are used for component 1. On this phase diagram vapor–liquid coexistence lines originate from pure component 1 ($x_2 = 0$, $T^* \equiv kT/\epsilon_{11} = 0.732$) and decrease in temperature with increasing fugacity fraction ξ_2. Solid(1)–liquid coexistence lines originate from pure component 1 ($x_2 = 0$, $T^* = 0.687$) and decrease in temperature with increasing fugacity fraction ξ_2. The liquid–vapor and solid(1)–liquid curves meet at $T^* = 0.6785$ and form a three-phase, solid(1)–liquid–vapor equilibrium line. Solid(1)–vapor coexistence lines originate from this three-phase line and decrease in temperature with increasing fugacity fraction ξ_2. Liquid–vapor coexistence lines originate from pure component 2 ($x_2 = 1$, $T^* = 0.505$) and increase in temperature with decreasing fugacity fraction ξ_2. The liquid–vapor and solid(1)–vapor curves meet at $T^* = 0.516$ and form another three-phase, solid(1)–liquid–vapor equilibrium line. Solid(1)–liquid lines originate from this three-phase line and decrease in temperature with increasing fugacity fraction ξ_2. Liquid–solid(2) coexistence lines originate from pure component 2 ($x_2 = 1$, $T^* = 0.429$) and decrease in temperature with decreasing fugacity fraction ξ_2. The solid(1)–liquid and liquid–solid(2) curves meet at $T^* = 0.420$ and form a eutectic. Below this temperature (not shown in Figure 1) solid(1) and solid(2) are in equilibrium.

The phase diagram in the T–x plane for $P^* = 0.01$ is shown in Figure 2. Here the vapor–liquid coexistence lines have shifted to higher temperatures and are detached from the solid–liquid coexistence region. On this phase diagram vapor–liquid coexistence lines originate from pure component 1 ($x_2 = 0$, $T^* = 0.884$) and decrease in temperature with increasing fugacity fraction ξ_2 until they reach the vapor–liquid coexistence temperature for pure component 2 ($x_2 = 1$, $T^* = 0.633$). A miscible liquid phase exists below the vapor–liquid curves. Solid(1)–liquid coexistence lines originate from pure component 1 ($x_2 = 0$, $T^* = 0.688$) and decrease in temperature with increasing fugacity fraction ξ_2. Liquid–solid(2) coexistence lines originate from pure component 2 ($x_2 = 1$, $T^* = 0.431$) and decrease in temperature with decreasing fugacity fraction ξ_2. The solid(1)–liquid and liquid–solid(2) curves meet at $T^* = 0.422$ and form a eutectic. Below this temperature (not shown in Figure 2) solid(1) and solid(2) are in equilibrium.

The phase diagram in the T–x plane for $P^* = 0.025$ is shown in Figure 3. This phase diagram is similar to the one for $P^* = 0.01$ shown in Figure 2, except that the vapor–liquid coexistence region appears at higher temperatures. The solid(1)–liquid and liquid–solid(2) curves meet at $T^* = 0.424$ and form a eutectic.

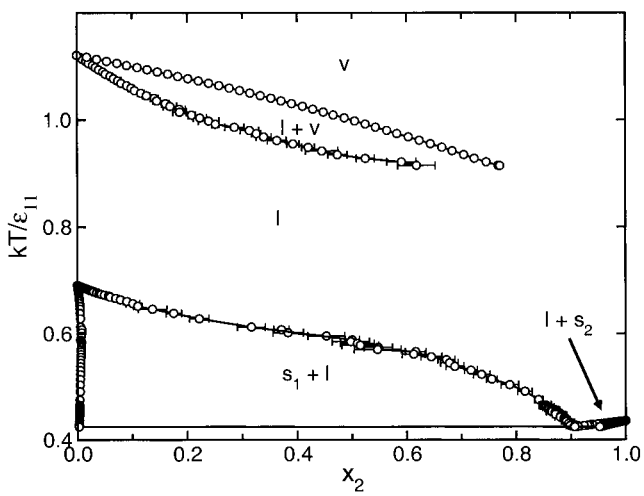

Figure 4. Temperature vs. composition-phase diagram for a binary Lennard-Jones mixture with diameter ratio σ_{11}/σ_{22} = 0.85 and $\epsilon_{11}/\epsilon_{22}$ = 1.6 at P^* = 0.05: symbols as in Figure 1.

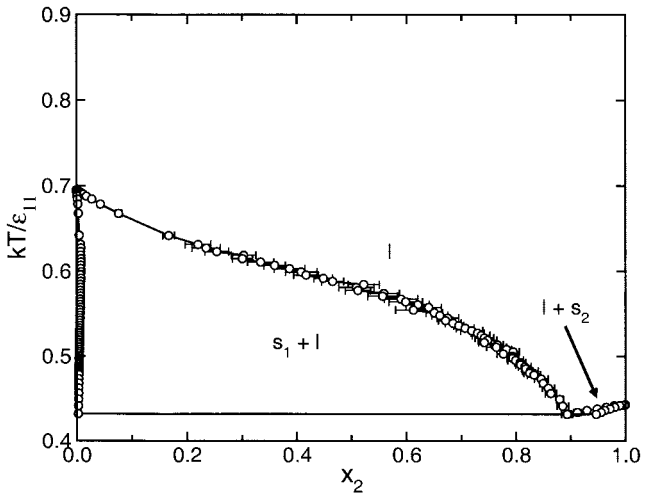

Figure 5. Temperature vs. composition-phase diagram for a Lennard-Jones binary mixture with diameter ratio $\sigma_{11}/\sigma_{22} = 0.85$ and $\epsilon_{11}/\epsilon_{22} = 1.6$ at $P^* = 0.1$: symbols as in Figure 1.

The phase diagram in the T–x plane for $P^* = 0.05$ is shown in Figure 4. The vapor–liquid coexistence region has again shifted to higher temperatures, but because this pressure is above the critical pressure for pure component 2 ($P_c^* = 0.0476$), the coexistence region ends at a mixture critical point instead of spanning the diagram from $x_2 = 0.0$ to $x_2 = 1.0$. During the Gibbs-Duhem integration simulation, the liquid phase vaporized as the system approached the liquid–vapor critical point. The present simulation method is not suitable for determining a mixture critical point because the correlation lengths for the density fluctuations diverge at the critical point and these fluctuations are restricted by the finite size of the simulation box (Frenkel and Smith, 1996). Instead finite-size scaling methods (Bruce and Wilding, 1992; Wilding and Bruce, 1992; Wilding, 1995; Potoff and Panagiotopoulos, 1998), which enable one to extract infinite-volume critical parameters from a simulation of finite size, must be employed to obtain accurate values of the critical point. We have not undertaken any finite-scaling analysis to determine the mixture critical point, but we estimate it to be in the vicinity of $T^* = 0.9$ and $x_2 = 0.7$. The solid(1)–liquid and liquid–solid(2) curves meet at $T^* = 0.425$ and form a eutectic.

The phase diagram in the T–x plane for $P^* = 0.1$ is shown in Figure 5. Attempts to calculate a vapor–liquid coexistence curve originating from the vapor–liquid equilibrium temperature of pure component 1 ($x_2 = 0$, $T^* = 1.261$) were unsuccessful because the liquid phase vaporizes as we step away from $x_2 = 0$ ($\xi_2 = 0$) during the Gibbs-Duhem integration. This is not surprising since this coexistence point is very near the critical temperature and pressure of pure component 1 ($T_c^* = 1.316$, $P_c^* = 0.124$). The solid(1)–liquid and liquid–solid(2) curves meet at $T^* = 0.432$ and form a eutectic.

To understand how variations in pressure lead to the complete phase diagrams displayed in Figures 1–5, it is helpful to consider the set of phase diagrams shown in Figure 6. The pure component solid–liquid coexistence temperatures and the eutectic temperature and composition are essentially unaffected by changes in pressure, while the pure-component vapor–liquid coexistence temperatures increase with increasing pressure. This is not surprising since liquids and solids are relatively incompressible and hence, their properties are not strongly affected by pressure. At $P^* = 0.002$, there is interference between the vapor–liquid and solid–liquid coexistence regions. As the pressure increases to $P^* = 0.01$, the pure-component vapor–liquid coexistence temperatures increase, shifting the entire vapor–liquid coexistence region to higher temperatures until it lifts off the solid–liquid coexistence region. At $P^* = 0.05$, we begin to enter the critical region for mixtures rich in component 2 and the vapor–liquid coexistence region begins to shrink away from the $x_2 = 1$ axis. Finally, at $P^* = 0.1$, the

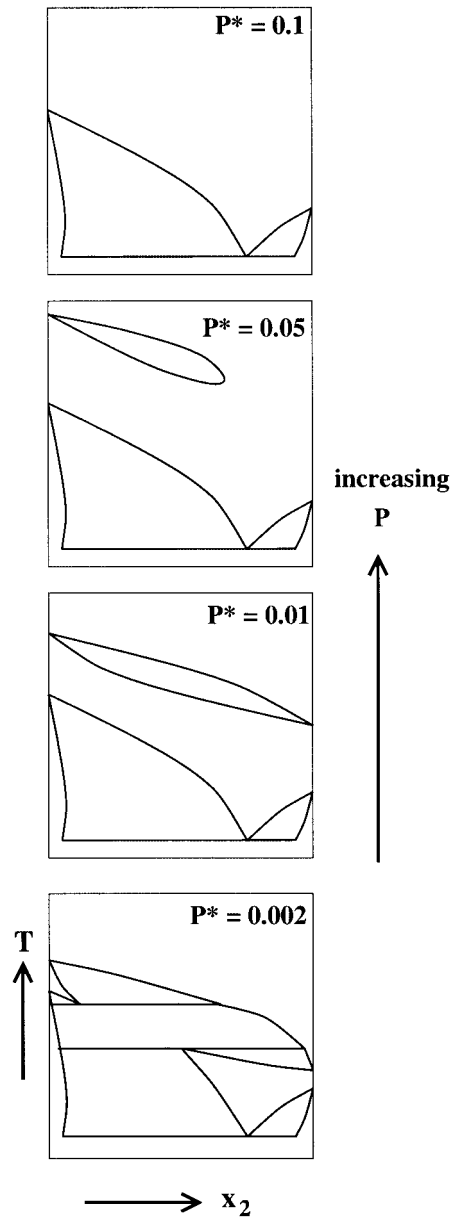

Figure 6. Temperature vs. composition-phase diagrams illustrating the effect of increasing pressure for the binary Lennard-Jones mixture with $\sigma_{11}/\sigma_{22} = 0.85$ and $\epsilon_{11}/\epsilon_{22} = 1.6$.

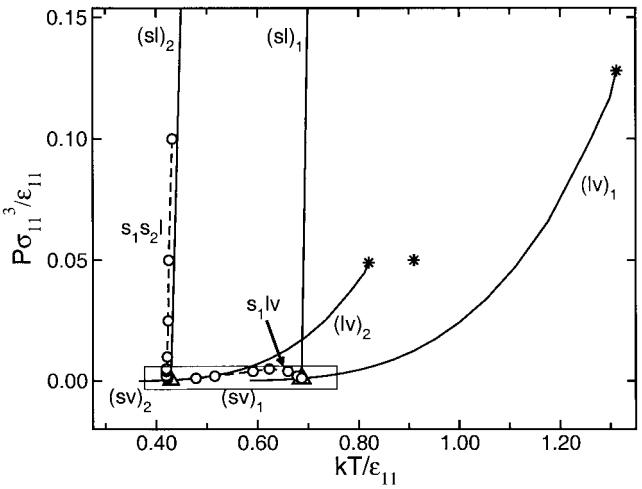

Figure 7. Pressure–temperature projection for a Lennard-Jones binary mixture with diameter ratio σ_{11}/σ_{22} = 0.85 and well-depth ratio $\epsilon_{11}/\epsilon_{22}$ = 1.6.

The region enclosed by the rectangle is enlarged in Figure 8. The open circles represent three-phase coexistence data determined from Gibbs-Duhem integration simulations. Dashed lines are drawn through the simulation points as a guide to the eye. The remaining symbols are as follows: solid lines represent the pure-component vapor pressure and melting curves, asterisks denote pure-component and mixture vapor–liquid critical points, open triangles denote pure-component triple points. The labels identifying the coexistence lines and points are as follows: $(lv)_i$, $(sl)_i$, $(sv)_i$ denote liquid–vapor, solid–liquid, and solid–vapor coexistence for pure component i; s_ilv denotes solid–liquid–vapor coexistence where the solid phase is an fcc solid solution rich in component i; s_1s_2l denotes solid(1)–solid(2)–liquid coexistence.

entire range of mixture compositions is in the critical region and the vapor–liquid coexistence region has disappeared.

P–T Projections for Binary Mixtures

In this section we present P–T projections for Lennard-Jones binary mixtures. To construct a P–T projection for a mixture, we first plot the pure-component coexistence data (taken from the work of Kofke and coworkers (Kofke, 1993; Agrawal and Kofke, 1995): vapor–liquid, solid–liquid, and solid–vapor equilibrium curves; vapor–liquid critical points; and solid–liquid–vapor triple points. We then use Gibbs-Duhem integration to calculate T–x diagrams at several pressures and plot all of the three-phase coexistence (s_1s_2l, s_1s_2v, s_2lv, s_1lv) temperatures and pressures on a P–T diagram.

To illustrate the construction of a P–T diagram, the results for the binary mixture with σ_{11}/σ_{22} = 0.85 and $\epsilon_{11}/\epsilon_{22}$ = 1.6 described earlier are given on the P–T projection shown in Figure 7. Our estimate of the binary-mixture critical point at P^* = 0.05 is shown by an asterisk. The solid(1)–solid(2)–liquid (s_1s_2l) and solid(1)–liquid–vapor (s_1lv) temperatures determined from the simulations in this work are shown by open circles, with dashed lines connecting the points to guide the eye. The eutectic (s_1s_2l) locus is relatively independent of pressure and can be found at approximately T^* = 0.425. Figure 8 shows a close-up of the region surrounding the pure-component triple points. Here, the solid(1)–liquid–vapor (s_1lv) coexistence line originates from the triple point of pure component 1 and passes through a maximum pressure of P^* = 0.005 at T^* = 0.62. A solid(1)–solid(2)–vapor coexistence line is drawn between the two s_1s_2v points found at P^* = 0.0002 and 0.00042 (the point at P^* = 0.00042 is nearly indistinguishable from the triple point at this scale). According to the phase rule (Findlay et al., 1951), a quadruple point (s_1s_2lv) is expected at the intersection of the s_1lv, s_2lv (not shown), s_1s_2l and s_1s_2v three-phase coexistence lines. Although we did not attempt the lengthy trial-and-error calculation needed to locate the quadruple point for this parameter set, it is apparent from Figure 8 that the quadruple point will be found in the vicinity of the triple point of pure component 2. In the same manner, we constructed P–T phase diagrams for binary mixtures with $\epsilon_{11}/\epsilon_{22}$ = 1.6 and σ_{11}/σ_{22} = 0.90 and 0.95, and $\epsilon_{11}/\epsilon_{22}$ = 0.45 and σ_{11}/σ_{22} = 0.85, 0.90, and 0.95, using results from several T–x calculations at pressures ranging from P^* = 0.0002 to 0.1. The P–T diagrams for these mixtures are shown in Figures 9–14.

In Figure 9, we show a P–T projection for the binary mixture with σ_{11}/σ_{22} = 0.9 and $\epsilon_{11}/\epsilon_{22}$ = 1.6. The solid(1)–solid(2)–liquid (s_1s_2l) locus is relatively independent of pressure and

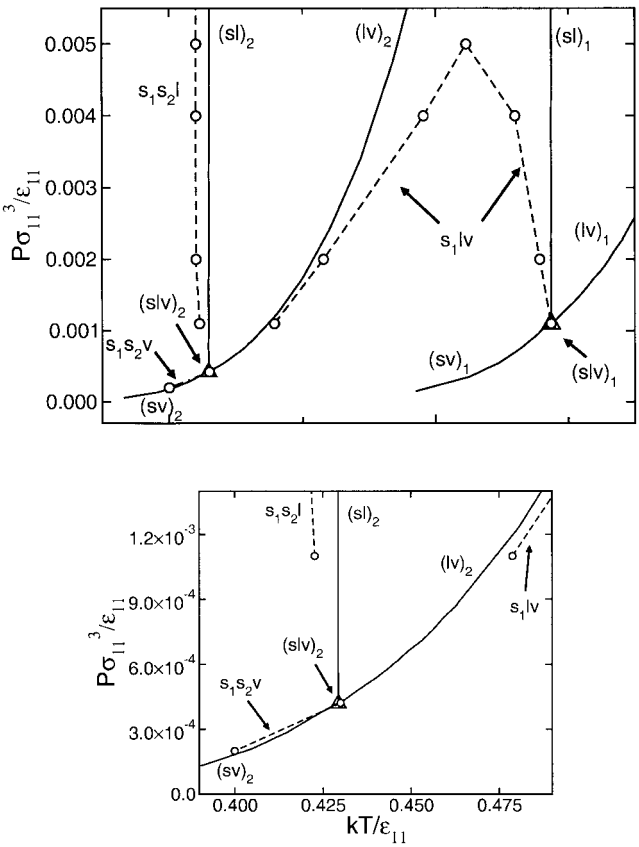

Figure 8. Close-up of the region surrounding the pure-component triple points for the pressure–temperature projection for a binary Lennard-Jones mixture with σ_{11}/σ_{22} = 0.85 and $\epsilon_{11}/\epsilon_{22}$ = 1.6.

The inset shows the region surrounding the triple point of pure component 2. The label s_1s_2v denotes solid(1)–solid(2)–vapor coexistence. Other symbols and labels as in Figure 7. $(slv)_i$ denotes solid-liquid vapor coexistence for pure component i.

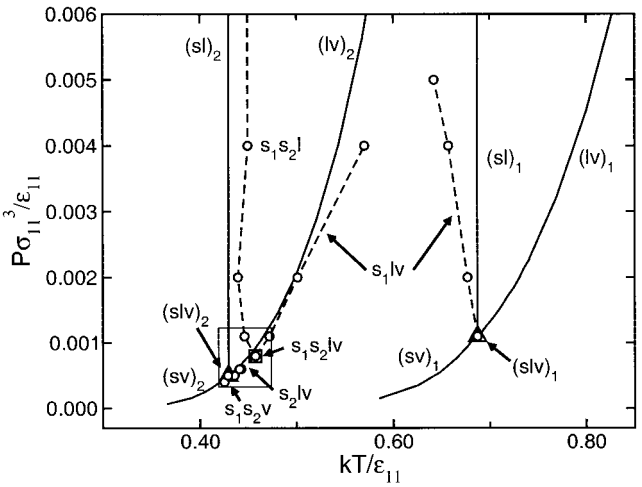

Figure 9. Pressure–temperature projection for a binary Lennard-Jones mixture with diameter ratio σ_{11}/σ_{22} = 0.90 and well-depth ratio $\epsilon_{11}/\epsilon_{22}$ = 1.6.

The region enclosed by the rectangle is enlarged in Figure 10. The open square represents a quadruple coexistence point determined from Gibbs-Duhem integration simulations. The label $s_1s_2$lv denotes solid(1)–solid(2)–liquid–vapor coexistence. Other symbols and labels as in Figures 7 and 8.

can be found at approximately $T^* = 0.45$. Two branches of the s_1lv locus are shown. The first branch originates from the triple point of pure component 1 and decreases in temperature with increasing pressure. We anticipate that this branch will eventually pass through a maximum pressure (not shown) and then join the second, low-temperature s_1lv branch, forming a continuous s_1lv coexistence line. Figure 10 gives a close-up view of the region surrounding the triple point of component 2. It can be seen that a s_1s_2lv quadruple point (denoted by the open square) exists at $T^* = 0.457$. This point was found

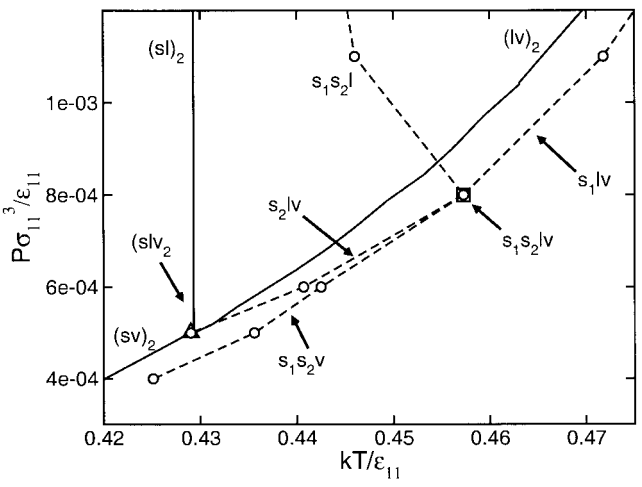

Figure 10. Close-up of the region surrounding the quadruple point for the pressure–temperature projection for a binary Lennard-Jones mixture with diameter ratio σ_{11}/σ_{22} = 0.90 and well-depth ratio $\epsilon_{11}/\epsilon_{22}$ = 1.6: symbols as in Figures 7, 8, and 9.

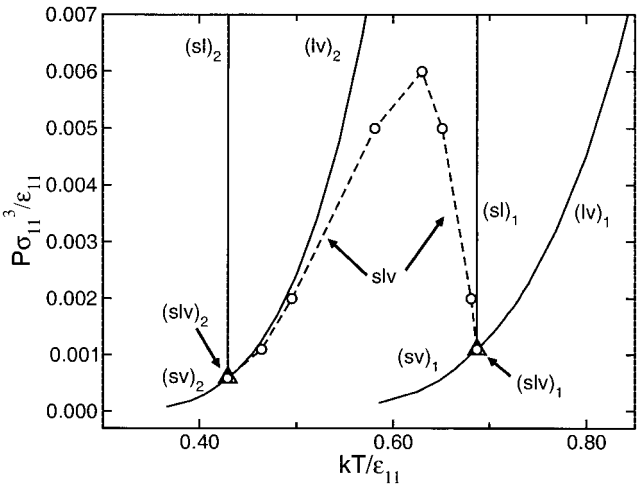

Figure 11. Pressure–temperature projection for a binary Lennard-Jones mixture with diameter ratio σ_{11}/σ_{22} = 0.95 and well-depth ratio $\epsilon_{11}/\epsilon_{22}$ = 1.6: symbols as in Figure 7.

during the T–x phase-diagram calculation at $P^* = 0.008$. As mentioned earlier, on a P–T projection, the quadruple point appears at the intersection of four, three-phase coexistence lines: s_1lv, s_2lv, s_1s_2l, and s_1s_2v. A line of s_2lv coexistence originates from the triple point of pure component 2 and terminates at the quadruple point. A line of s_1s_2v coexistence originates from $P^* = 0.0004$ (the lowest pressure considered for this system) and terminates at the quadruple point.

In Figure 11, for the binary mixture with $\sigma_{11}/\sigma_{22} = 0.95$ and $\epsilon_{11}/\epsilon_{22} = 1.6$, an slv coexistence line originates from the triple point of pure component 1 and decreases in temperature with increasing pressure, passing through a maximum pressure and then decreasing in temperature with decreasing pressure until it terminates at the triple point of pure component 2. No solid–solid immiscibility was observed for this mixture at the pressures considered.

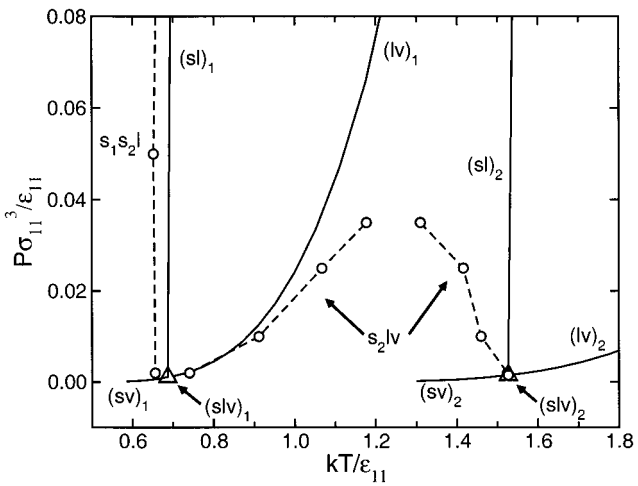

Figure 12. Pressure–temperature projection for a binary Lennard-Jones mixture with diameter ratio σ_{11}/σ_{22} = 0.85 and well-depth ratio $\epsilon_{11}/\epsilon_{22}$ = 0.45: symbols as in Figure 7.

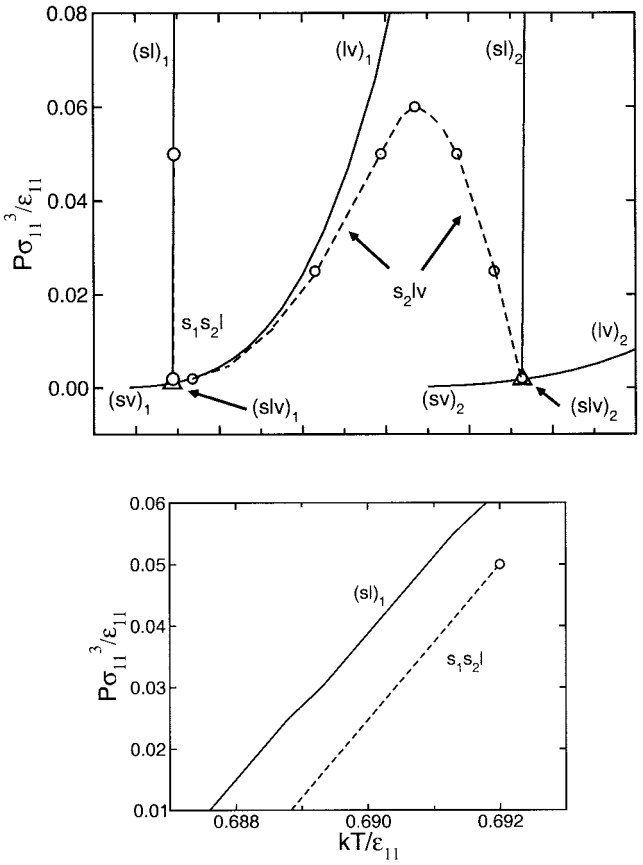

Figure 13. Pressure–temperature projection for a binary Lennard-Jones binary mixture with diameter ratio $\sigma_{11}/\sigma_{22} = 0.90$ and well-depth ratio $\epsilon_{11}/\epsilon_{22} = 0.45$.

The inset shows the solid(1)–solid(2)–liquid coexistence line. Symbols as in Figure 7.

Looking at Figures 8, 9, and 11, we see that as the diameter ratio increases, the vapor–liquid and solid–liquid interference continues to higher pressures (as indicated by the maximum pressure in the s_1lv curve on the P–T diagrams). Additionally, the locus of solid–solid–liquid temperatures shifts from temperatures below both pure component melting points at $\sigma_{11}/\sigma_{22} = 0.85$ to temperatures above the pure-component-1 melting point at $\sigma_{11}/\sigma_{22} = 0.90$, changing the characteristic shape of the solid–liquid coexistence region from eutectic to peritectic. Finally, at $\sigma_{11}/\sigma_{22} = 0.95$ the solid–solid immiscibility region disappears and the solid phase exists as a solid solution.

In Figure 12, for the binary mixture with $\sigma_{11}/\sigma_{22} = 0.85$ and $\epsilon_{11}/\epsilon_{22} = 0.45$, the eutectic ($s_1s_2l$) locus is relatively independent of pressure and can be found at approximately $T^* = 0.655$. Two branches of the s_2lv locus are shown. The first branch originates from the triple point of pure component 2 and decreases in temperature with increasing pressure. We anticipate that this branch will eventually pass through a maximum pressure (not shown) and then join the second, low-temperature s_2lv branch, forming a continuous s_2lv coexistence line that ends at a quadruple point. We did not attempt the lengthy trial-and-error calculation needed to locate the quadruple point for this parameter set, but it is apparent from Figure 12 that the quadruple point will be found in the vicinity of the triple point of pure component 1. A similar pattern of phase behavior was observed for the mixtures with $\sigma_{11}/\sigma_{22} = 0.90$ and 0.95, shown in Figures 13 and 14, where the s_2lv coexistence line begins at the triple point of pure component 2, passes through a maximum pressure, and ends at a quadruple point (not calculated for these mixtures). The inset of Figure 13 shows that the s_1s_2l locus for the mixture with $\sigma_{11}/\sigma_{22} = 0.90$ and $\epsilon_{11}/\epsilon_{22} = 0.45$ appears at higher temperatures than the solid–liquid coexistence line for component 1, meaning that the s_1s_2l equilibria are of the peritectic type. Thus, we see that as the diameter ratio increases, the vapor–liquid and solid–liquid interference (as indicated by the maximum pressure in the s_2lv curve) persists at higher pressures. Additionally, the locus of solid–solid–liquid temperatures shifts from temperatures below both pure component melting points at $\sigma_{11}/\sigma_{22} = 0.85$ to temperatures above the pure-component-1 melting point at $\sigma_{11}/\sigma_{22} = 0.95$, changing the characteristic shape of the solid–liquid coexistence region from eutectic to peritectic.

Upon comparing the phase diagrams shown in Figures 7 and 12 for the mixtures with $\sigma_{11}/\sigma_{22} = 0.85$ and $\epsilon_{11}/\epsilon_{22} = 0.45$ and 1.6, we find that decreasing the well-depth ratio causes the coexistence curves for pure component 2 to shift from temperatures lower than those for pure component 1 to temperatures higher than those for pure component 1. At $\epsilon_{11}/\epsilon_{22} = 1.6$, the vapor–liquid and solid–liquid interference ends, that is, the slv curve disappears near $P^* = 0.005$, but for $\epsilon_{11}/\epsilon_{22} = 0.45$, the vapor–liquid and solid–liquid interference ends near $P^* = 0.04$. Thus, we conclude that as $\epsilon_{11}/\epsilon_{22}$ decreases the maximum pressure in the slv locus decreases.

Summary

The Gibbs-Duhem integration technique was combined with semigrand canonical Monte Carlo simulations to calculate complete phase diagrams for binary Lennard-Jones mixtures at several different pressures to explore the effects of molecular size, intermolecular attractions, and pressure on the complete

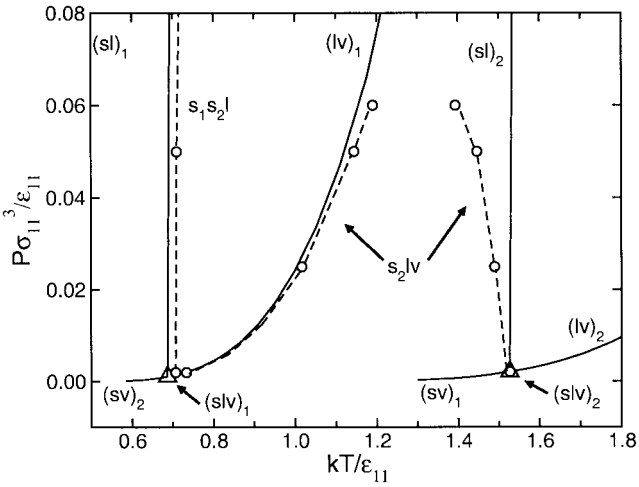

Figure 14. Pressure–temperature projection for a binary Lennard-Jones mixture with diameter ratio $\sigma_{11}/\sigma_{22} = 0.95$ and well-depth ratio $\epsilon_{11}/\epsilon_{22} = 0.45$: symbols as in Figure 7.

phase behavior of a mixture. We calculated T–x phase diagrams for binary Lennard-Jones mixtures with diameter ratios ranging from 0.85 to 0.95, and attractive well-depth ratios of 0.45 and 1.6 at reduced pressures ranging from $P^* = 0.0002$ to 0.1. We then constructed a P–T phase diagram for each mixture.

The procedure described here and in Lamm and Hall (2001) provides a protocol for probing the complete phase equilibria of a mixture. In principle, the Gibbs-Duhem integration approach is not limited to the study of simple molecular fluids with spherically symmetric potentials. However, obtaining the initial coexistence condition required to commence a Gibbs-Duhem integration simulation is not always a trivial undertaking, especially for polymers and other complex fluids. Recently, some new methods have been proposed for calculating phase coexistence at individual values of temperature and pressure. In one approach by Silva Fernandes et al. (2001), a Gibbs ensemble simulation (Panagiotopoulos, 1987) of vapor–liquid coexistence in a one-component fluid is conducted at successively lower temperatures. The triple point (solid–liquid–vapor) of the substance is inferred by locating the temperature where the liquid phase becomes unstable and spontaneously freezes. A second approach by Chen et al. (2001) uses a modified Gibbs ensemble method to determine solid–vapor, solid–liquid–vapor, and solid–solid–vapor phase coexistence in a substance. Unlike the original Gibbs ensemble implementation, where each phase is given a simulation box and remains in thermodynamic contact with the other phases through particle exchange moves, in this method the box containing the solid is elongated and contains a slab of solid material surrounded by a vapor phase. Finally, a class of methods utilizing virtual Gibbs ensembles have been introduced by Escobedo and coworkers (Escobedo, 1999; Shetty and Escobedo, 2002) to calculate solid–fluid coexistence. Configurational bias Monte Carlo moves (Martin and Siepmann, 1999) could be combined with any of these methods to facilitate the generation of initial coexistence conditions of asymmetric or chainlike molecules for subsequent use in Gibbs-Duhem integration simulations.

Acknowledgments

This work was supported by the GAANN Computational Sciences Fellowship of the U.S. Department of Education and the Office of Energy Research, Basic Sciences, Chemical Science Division of the U.S. Department of Energy under Contract No. DE-FG05-91ER14181. Acknowledgment is made to the Donors of the Petroleum Research Fund administered by the American Chemical Society for partial support of this work. We thank D. Kofke for helpful discussions on the Gibbs Duhem integration method.

Literature Cited

Agrawal, R., and D. A. Kofke, "Thermodynamic and Structural Properties of Model Systems at Solid-Fluid Coexistence. II. Melting and Sublimation of the Lennard-Jones System," *Mol. Phys.,* **85,** 43 (1995).

Allen, M. P., and D. J. Tildesley, *Computer Simulation of Liquids,* Clarendon Press, Oxford (1987).

Barrat, J. L., M. Baus, and J. P. Hansen, "Density-Functional Theory of Freezing of Hard-Sphere Mixtures in Substitutional Solid Solutions," *Phys. Rev. Lett.,* **56,** 1063 (1986).

Barrat, J. L., M. Baus, and J. P. Hansen, "Freezing of Hard-Sphere Mixtures into Disordered Crystals: A Density-Functional Approach," *J. Phys. C: Solid State Phys.,* **20,** 1413 (1987).

Bruce, A. D., and N. B. Wilding, "Scaling Fields and Universality of the Liquid-Gas Critical Point," *Phys. Rev. Lett.,* **68,** 193 (1992).

Carnahan, B., H. A. Luther, and J. O. Wilkes, *Applied Numerical Methods,* Wiley, New York (1969).

Chen, B., J. I. Siepmann, and M. L. Klein, "Direct Gibbs ensemble Monte Carlo Simulations for Solid-Vapor Phase Equilibria: Applications to Lennard-Jonesium and Carbon Dioxide," *J. Phys. Chem. B,* **105,** 9840 (2001).

Cottin, X., and P. A. Monson, "Substitutionally Ordered Solid Solutions of Hard Spheres," *J. Chem. Phys.,* **102,** 3354 (1995).

Escobedo, F. A., "Tracing Coexistence Lines in Multicomponent Fluid Mixtures by Molecular Simulation," *J. Chem. Phys.,* **110,** 11999 (1999).

Findlay, A., A. N. Campbell, and N. O. Smith, *The Phase Rule and Its Applications,* Dover, New York (1951).

Frenkel, D., and B. Smit, *Understanding Molecular Simulations,* Academic Press, San Diego (1996).

Garcia, D. C., and K. D. Luks, "Patterns of Solid-Fluid Phase Equilibria: New Possibilities?" *Fluid Phase Equilib.,* **161,** 91 (1999).

Hansen, J. P., and L. Verlet, "Phase Transitions of the Lennard-Jones System," *Phys. Rev.,* **184,** 151 (1969).

Hitchcock, M. R., and C. K. Hall, "Solid-Liquid Phase Equilibrium for Binary Lennard-Jones Mixtures," *J. Chem. Phys.,* **110,** 11433 (1999).

Kofke, D. A., "Solid-Fluid Coexistence in Binary Hard Sphere Mixtures by Semigrand Monte Carlo Simulation," *Mol. Simul.,* **7,** 285 (1991).

Kofke, D. A., "Direct Evaluation of Phase Coexistence by Molecular Simulation via Integration Along the Saturation Line," *J. Chem. Phys.,* **98,** 4149 (1993).

Kofke, D. A., "Semigrand Canonical Monte Carlo Simulation. Integration Along Coexistence Lines," *Adv. Chem. Phys.,* **105,** 405 (1998).

Kofke, D. A., and E. D. Glandt, "Monte Carlo Simulations of Multicomponent Equilibria in a Semigrand Canonical Ensemble," *Mol. Phys.,* **64,** 1105 (1988).

Kranendonk, W. G. T., and D. Frenkel, "Computer Simulation of Solid-Liquid Coexistence in Binary Hard-Sphere Mixtures," *Mol. Phys.,* **72,** 679 (1991).

Labadie, J. A., D. C. Garcia, and K. D. Luks, "Patterns of Solid-Fluid Phase Equilibria II. Interplay with Fluid Phase Criticality and Stability," *Fluid Phase Equilib.,* **171,** 11 (2000).

Lamm, M. H., and C. K. Hall, "Molecular Simulation of Complete Phase Diagrams for Binary Mixtures," *AIChE J.,* **47,** 1664 (2001).

Luks, K. D., "Experimental Techniques in Solid-Liquid Equilibrium," *Proc. Int. Conf. on Phase Equilibria and Fluid Properties in the Chemical Industry,* EFCE Series No. 11, Part II, 699 (1980).

Martin, M. G., and J. I. Siepmann, "Novel Configurational-Bias Monte Carlo Method for Branched Molecules. Transferable Potentials for Phase Equilibria. 2. United-Atom Description of Branched Alkanes," *J. Phys. Chem. B,* **103,** 4508 (1999).

Mehta, M., and D. A. Kofke, "Coexistence Diagrams of Mixtures by Molecular Simulation," *Chem. Eng. Sci.,* **49,** 2633 (1994).

Panagiotopoulos, A. Z., "Direct Determination of Phase Coexistence Properties of Fluids by Monte Carlo Simulation in a New Ensemble," *Mol. Phys.,* **61,** 813 (1987).

Peters, C. J., R. N. Lichtenhaler, and J. de Swaan Arons, "Three Phase Equilibria in Binary Mixtures of Ethane and Higher Alkanes," *Fluid Phase Equilib.,* **29,** 495 (1986).

Potoff, J. J., and A. Z. Panagiotopoulos, "Critical Point and Phase Behavior of the Pure Fluid and a Lennard-Jones Mixture," *J. Chem. Phys.,* **109,** 10914 (1998).

Prausnitz, J. M., R. N. Lichtenhaler, and E. Gomes de Azevedo, *Molecular Thermodynamics of Fluid-Phase Equilibria,* Prentice Hall, Englewood Cliffs, NJ (1986).

Rowlinson, J. S., and F. L. Swinton, *Liquids and Liquid Mixtures,* Butterworth Scientific, London (1982).

Schneider, G. M., "Phase Equilibria in Fluid Mixtures at High Pressures," *Adv. Chem. Phys.,* **17,** 1 (1970).

Schneider, G. M., "High-Pressure Phase Diagrams and Critical Properties of Fluid Mixtures," *Chemical Thermodynamics,* Vol. 2, *Specialist Periodical Report,* M. L. McGlashan, ed., The Chemical Society, London (1978).

Scott, R. L., "Models for Phase Equilibria in Fluid Mixtures," *Acc. Chem. Res.,* **20,** 97 (1987).

Shetty, R., and F. A. Escobedo, "Tracing Coexistence Lines in Multicomponent Fluid Mixtures by Molecular Simulation," *J. Chem. Phys.,* **116,** 7957 (2002).

Silva Fernandes, F. M. S., R. P. S. Fartaria, and F. F. M. Freita, "The Starting State in Simulations of the Fluid-Solid Coexistence by Gibbs-Duhem Integration," *Comput. Phys. Commun.,* **141,** 403 (2001).
Valyashko, V. M., "Complete Phase Diagrams of Binary Systems with Different Volatility Components," *Z. Phys. Chem. (Leipzig),* **267,** 481 (1986).
Valyashko, V. M., "Sub- and Supercritical Equilibria in Aqueous Electrolyte Solutions," *Pure Appl. Chem.,* **62,** 2129 (1990).
Wilding, N. B., "Critical-Point and Coexistence-Curve Properties of the Lennard-Jones Fluid: A Finite-Size Scaling Study," *Phys. Rev. E,* **52,** 602 (1995).
Wilding, N. B., and A. D. Bruce, "Density Fluctuations and Field Mixing the Critical Field," *J. Phys. Cond. Mat.,* **4,** 3087 (1992).

Appendix

Here we derive the Clapeyron differential equation for a binary mixture shown in Eq. 1. We begin by writing the Gibbs-Duhem equation (Prausnitz et al., 1986) for any extensive property, $M(T, P, n_1, n_2, \cdots)$

$$(\partial M/\partial T)_{P,\text{ all } n}\, dT + (\partial M/\partial P)_{T,\text{ all } n}\, dP - \sum n_i d\bar{m}_i = 0 \quad \text{(A1)}$$

where T is the absolute temperature, P is the pressure, n_i is the number of moles of component i, and $\bar{m}_i \equiv (\partial M/\partial n_i)_{T,P,n_j}$ is the partial molar property of component i. Letting $M = G/(kT)$, where G is the total Gibbs free energy of the system and k is the Boltzmann constant, and using the fundamental relation, $dG = -SdT + VdP + \sum \mu_i dn_i$, where S and V are the total entropy and volume, and $\mu_i \equiv \bar{g}_i \equiv (\partial G/\partial n_i)_{T,P,n_j}$ is the chemical potential of component i, we obtain

$$-H/(kT^2)\, dT + V/(kT)\, dP - \sum n_i d(\mu_i/(kT)) = 0 \quad \text{(A2)}$$

where H is the total enthalpy of the system and we have used the Gibbs-Helmholtz relation, $(\partial(G/(kT))/\partial T)_{P,n_i} = -H/(kT^2)$. Equation A2 can be simplified by dividing by the total number of moles and defining a reciprocal temperature, $\beta = 1/(kT)$ to obtain

$$hd\beta + \beta v dP = \sum x_i d(\beta\mu_i) \quad \text{(A3)}$$

where h and v are the molar enthalpy and molar volume, respectively, and x_i is the mole fraction of component i. Considering the case of constant pressure, Eq. A3 reduces to

$$hd\beta = \sum x_i\, d(\beta\mu_i). \quad \text{(A4)}$$

For our purposes it is more convenient (Mehta and Kofke, 1994) to express Eq. A4 in terms of the fugacity, $\hat{f}_i$, and the fugacity fraction, $\xi_i \equiv \hat{f}_i/\sum \hat{f}_i$ of component i. We rewrite the chemical potential in terms of the fugacity, $d\mu_i = kTd \ln \hat{f}_i$, and substitute this expression into Eq. A4 to obtain

$$hd\beta = \sum x_i\, d \ln \hat{f}_i \quad \text{(A5)}$$

We then add and subtract $\sum x_i\, d \ln(\sum \hat{f}_i)$ to the lefthand side of Eq. A5 and rearrange to obtain

$$\sum x_i\, d \ln\left(\sum \hat{f}_i\right) = h\, d\beta - \sum x_i\, d \ln\left(\frac{\hat{f}_i}{\sum \hat{f}_i}\right) = h\, d\beta - \sum x_i\, d \ln \xi_i \quad \text{(A6)}$$

The lefthand side of Eq. A6 is simplified by taking the term $d \ln(\sum \hat{f}_i)$ outside of the summation and recognizing that $\sum x_i = 1$. By the chain rule for differentiation, $d \ln \xi_i = (1/\xi_i)\, d\xi_i$ and substituting for $d \ln \xi_i$ in Eq. A6 we obtain the isobaric Gibbs-Duhem equation in terms of the fugacity fraction

$$d \ln\left(\sum \hat{f}_i\right) = h\, d\beta - \sum \frac{x_i}{\xi_i} d\xi_i \quad \text{(A7)}$$

To obtain the Clapeyron differential equation, consider two coexisting phases, α and γ. Equation A7 holds for each phase

$$d \ln\left(\sum \hat{f}_i^{\alpha}\right) = h^{\alpha}\, d\beta - \sum \frac{x_i^{\alpha}}{\xi_i^{\alpha}} d\xi_i^{\alpha} \quad \text{(A8a)}$$

and

$$d \ln\left(\sum \hat{f}_i^{\gamma}\right) = h^{\gamma}\, d\beta - \sum \frac{x_i^{\gamma}}{\xi_i^{\gamma}} d\xi_i^{\gamma} \quad \text{(A8b)}$$

At equilibrium, $d \ln(\sum \hat{f}_i^{\alpha}) = d \ln(\sum \hat{f}_i^{\gamma})$ and $\xi_i^{\alpha} = \xi_i^{\gamma}$. Subtracting Eq. A8b from Eq. A8a gives

$$0 = (h^{\alpha} - h^{\gamma})\, d\beta - \sum \frac{(x_i^{\alpha} - x_i^{\gamma})}{\xi_i} d\xi_i \quad \text{(A9)}$$

where we have dropped the superscripts α and γ on the fugacity fraction ξ_i. This equation shows how temperature and fugacity fraction must vary along the coexistence line to maintain equilibrium between phases α and γ. For a binary system consisting of species 1 and 2, Eq. A9 becomes

$$\frac{x_1^{\alpha} - x_1^{\gamma}}{\xi_1} d\xi_1 + \frac{x_2^{\alpha} - x_2^{\gamma}}{\xi_2} d\xi_2 = (h^{\alpha} - h^{\gamma})\, d\beta \quad \text{(A10)}$$

From the definition of mole fraction and fugacity fraction we write $x_1 = 1 - x_2$, $\xi_1 = 1 - \xi_2$, and $d\xi_1 = -d\xi_2$. Substituting for x_1, ξ_1, and $d\xi_1$ in Eq. A10 and rearranging, gives

$$\frac{d\beta}{d\xi_2} = \frac{(x_2^{\alpha} - x_2^{\gamma})}{\xi_2(1 - \xi_2)(h^{\alpha} - h^{\gamma})}. \quad \text{(A11)}$$

Manuscript received Jan. 2, 2003, and revision received June 9, 2003.